Monthly Notices
of the
ROYAL ASTRONOMICAL SOCIETY

MNRAS **464,** 48–64 (2017) doi:10.1093/mnras/stw2100

The shape of dark matter haloes – IV. The structure of stellar discs in edge-on galaxies

S. P. C. Peters,[1] G. de Geyter,[2] P. C. van der Kruit[1]★ and K. C. Freeman[3]

[1]*Kapteyn Astronomical Institute, University of Groningen, PO Box 800, NL-9700AV Groningen, the Netherlands*
[2]*Sterrenkundig Observatorium, Universiteit Gent, Krijgslaan 281-S9, B-9000 Gent, Belgium*
[3]*Research School of Astronomy and Astrophysics, The Australian National University, Cotter Road Weston Creek, ACT 2611, Australia*

Accepted 2016 August 19. Received 2016 August 17; in original form 2015 July 23

ABSTRACT

We present optical and near-infrared archival observations of eight edge-on galaxies. These observations are used to model the stellar content of each galaxy using the FITSKIRT software package. Using FITSKIRT, we can self-consistently model a galaxy in each band simultaneously while treating for dust. This allows us to measure accurately both the scalelength and scale-height of the stellar disc, plus the shape parameters of the bulge. By combining these data with the previously reported integrated magnitudes of each galaxy, we can infer their true luminosities. We have successfully modelled seven out of the eight galaxies in our sample. We find that stellar discs can be modelled correctly, but we have not been able to model the stellar bulge reliably. Our sample consists for the most part of slowly rotating galaxies and we find that the average dust layer is much thicker than is reported for faster rotating galaxies.

Key words: galaxies: haloes – galaxies: kinematics and dynamics – galaxies: photometry – galaxies: spiral – galaxies: structure.

1 INTRODUCTION

This is the fourth article in a series of five in which we try to constrain the flattening of dark matter haloes from observations of the thickness and velocity dispersion of the H I layer in edge-on late-type dwarf galaxies. For this analysis, we need to correct for the influence of the stellar disc on the dynamics of the gas and therefore in this article we provide fits to the light distribution in the stellar discs of our sample galaxies.

Edge-on galaxies offer a unique perspective on the distribution of stars and dust in galaxies. A major advantage of the edge-on view is the ability to resolve the vertical distribution of both stars and dust; this is exactly the reason that in this series of articles we study edge-ons. A well-known feature of edge-on spiral galaxies is truncations at the outer edges of their stellar discs, as discovered in edge-on galaxies back in 1979 (van der Kruit 1979). Subsequent authors have confirmed the presence of truncations, for example the study of 34 edge-on galaxies by Kregel, van der Kruit & de Grijs (2002a), who found that at least 20 of these galaxies (∼60 per cent of the sample) have truncations. Not all galaxies are truncated. Some even appear to have an upturn in their radial profiles (Erwin, Pohlen & Beckman 2008), although van der Kruit & Freeman (2011) noted that many of these, e.g. NGC 3310, show signs of merging or other distortions in the outer parts. Some galaxies extend out to many scalelengths, such as NGC 300 (Bland-Hawthorn et al. 2005). In this series of articles, we do not concern ourselves with the outer features, as we model H I only in the inner parts in order to set limits on the three-dimensional shape of dark matter haloes. In Paper V, we determine the radius out to which we feel our data justify fitting for the shape of the dark matter haloes; the actual radii adopted for analysis vary from less than 1 up to typically 4 or 5 scalelengths, so we do not go out into these areas of extended stellar discs or upturns. Also, if any of our systems has a truncation, our analysis is restricted to the areas within that truncation.

A major drawback to the edge-on perspective is the more complex geometry, which implies that each position x along the major axis is a superposition of light emitted at a range of radii R. Various authors have therefore set out to disentangle edge-on galaxies and extract their radial structure. One approach to this is to deproject the edge-on image using the inverse Abel transform (Binney & Tremaine 1987). This method was first applied by Florido et al. (2001, 2006) in a study of the mid-plane of edge-on galaxies in the near-infrared. Pohlen et al. (2007) extended the method to study both the radial and vertical distribution of 11 edge-on galaxies. UGC 7321 was studied in this way by O'Brien, Freeman & van der Kruit (2010).

Dust can seriously hamper this type of deprojection, as there is no simple way to incorporate its complex interplay of scattering, absorption and emission in the inverse Abel transform. An alternative strategy for deriving the radial properties of the galaxy is to model the entire galaxy, including the dust. By using appropriate fitting algorithms, the model can be tweaked in various ways until it matches the observations. Various authors, such as Xilouris et al. (1999) and Bianchi (2007), have applied this method to edge-on galaxies.

★E-mail: vdkruit@astro.rug.nl

FITSKIRT was developed by de Geyter et al. (2013) as an automatic fitting extension for the SKIRT 3D-continuum Monte Carlo radiative transfer code (Baes & Dejonghe 2001a,b; Baes et al. 2003, 2011). FITSKIRT makes use of the GALIB genetic algorithm to fit a parametrized model of a galaxy (Wall 1996). In the so-called oligochromatic mode, the code can fit multiple bands simultaneously. This mode was used by de Looze et al. (2012) to model edge-on galaxy NGC 4565 from the UV to the mid-infrared in a self-consistent manner. This method has been applied by de Geyter et al. (2014) to a set of 12 edge-on galaxies selected from the Calar Alto Legacy Integral Field Area Survey (CALIFA).

In a previous article (Paper III in this series), we have modelled the H I structure and kinematics of eight edge-on dwarf galaxies, as part of our project to model their dark matter halo by inferring its properties from the baryonic content. In the current article, we continue this project by modelling the stellar and dust components of these eight edge-on galaxies. We have collected a large set of observations, which we present in Section 2. The models and strategy by which we fit the data are presented in Section 3. The fits to the data using FITSKIRT are presented in Section 4, after which we discuss the results in Section 5 and conclude the article in Section 6.

2 DATA

FITSKIRT can model observations ranging from the UV to the infrared. The more bands are available to it, the better the models can be constrained. In this article, we continue the analysis of the eight edge-on galaxies from the previous articles in the series. See table 2 in Paper I for an overview of the sample. In order to obtain the largest data set, a wide range of archives, both online and offline, has been explored. For most galaxies, a large set of archived observations were found. Unfortunately, the signal-to-noise ratio in many of these (survey) observations was insufficient, as the low-surface-brightness nature of most of these galaxies necessitated longer exposure times than were used. In total, we use data from 10 telescopes in nine bands, giving a minimum of three bands per galaxy and a maximum of nine. A full overview of the observations that we used is shown in Table A1 in the online Appendix.

2.1 Data reduction

FITSKIRT does not require the data to be calibrated, so we skipped that step in the reduction. As our observations come from a wide range of telescopes, each required its own appropriate treatment.

(i) **2.3-m ANU Advanced Technology Telescope**

The 2.3-m ANU Advanced Technology Telescope with the CASPIR near-IR camera, located at Siding Spring Observatory in Australia, was used to observe several of the galaxies in the *Kn* and *H* bands. The data were archived on tape and were originally intended for use in O'Brien et al. (2010). The CASPIR instrument has dedicated software for reducing the data, which suffered from code-rot and did not work correctly any more. With support from Peter McGregor at the Research School of Astronomy & Astrophysics in Canberra, Australia, along with the manual and source code for CASPIR, we managed to reconstruct the required workflow and re-implement this in PYTHON.

During an observing run, various types of observations are being made: bias, dark, flat, sky and object. First, we create the combined bias frame and subtract this from all other types of frame. CASPIR has a non-linear response and it was thus necessary to linearize the flat, dark sky and object frames. The dark currents were then removed from the sky, object and flat frames, after which the sky and object frames were flat-fielded. The sky in the near-infrared is bright and varies rapidly. The main observations were therefore taken as one short object frame followed by a sky frame. The sky frames before and after each object frame were used to subtract the sky from a particular object frame. The field of view of CASPIR only covers a fraction of a galaxy, so a dithering pattern was used to cover the entire galaxy. The information on the exact dithering pattern was unavailable and we thus resorted to calibrating the coordinate system of each frame manually, using IRAF. Each galaxy consisted of more than 50 object frames. Afterwards we use the MONTAGE toolkit[1] to create a montage of all these frames automatically. This process automatically performs background rectification between the various frames.

(ii) **3.9-m Anglo-Australian Telescope**

The IRIS2 instrument on the 3.9-m Anglo-Australian Telescope, located at Siding Spring Observatory in Australia, was used for various *Ks*- and *H*-band observations. Observations were available on tape and were originally intended for use in O'Brien et al. (2010). In contrast to the 2.3-m ANU Advanced Technology Telescope observations, the field of view is much larger and covers the entire galaxy and the surrounding patch of sky. The IRIS2 instrument has custom software, which automatically runs through the entire workflow and returns the reduced science-ready frame.

(iii) **ANU 40-inch telescope**

The Australian National University (ANU) 40-inch telescope, located at Siding Spring Observatory in Australia, was used to observe several of our galaxies, as intended for use in O'Brien et al. (2010). The data were archived on tapes. The traditional IRAF workflow of bias and flat-fielding removal was performed to reduce the data.

(iv) **CTIO 0.9-m telescope**

The *R*-band image for ESO 115–G021 was taken using the 0.9-m telescope located at the Cerro Tololo Inter-American Observatory (CTIO) in Chile. The observation was taken as part of the *Spitzer* Local Volume Legacy project and was provided science-ready online at the NASA/IPAC Extragalactic Database (NED).[2]

(v) **Danish 1.54-m telescope**

The Danish 1.54-m telescope is located at the European Southern Observatory (ESO) La Silla site in Chile. The *R*-band image for ESO 274–G001 was previously published by Rossa & Dettmar (2003) and was available science-ready online via NED.

(vi) **ESO 1-m Schmidt telescope**

The ESO–LV survey Lauberts & Valentijn (1988) digitized 606 blue and 606 red ESO photographic survey plates. The data were available science-ready through NED.

(vii) **ESO La Silla Schmidt telescope**

The ESO red-band survey has been digitized using the Multi-Anode Microchannel Array microdensitometer and provided as science-ready data, available through a virtual-observatory (VO) interface. These images were originally part of the ESO(B) Atlas, taken with the ESO 1-m Schmidt telescope at La Silla, Chile (Lauberts 1982).

(viii) **Palomar 48-inch Schmidt telescope**

The 48-inch Schmidt telescope at Palomar Observatory in the United States was used to create the Palomar Sky Survey (POSS). This survey was later digitized into the Digitized Sky Survey (DSS). The data were provided science-ready through a VO interface.

[1] Available at http://montage.ipac.caltech.edu/
[2] Available at http://ned.ipac.caltech.edu/

(ix) ***Spitzer*Space Telescope IRAC**
The *Spitzer* Space Telescope archive had 3.6-μm observations of all our galaxies and for several also 4.5-μm observations. The observations were taken for a range of projects (Engelbracht et al. 2008; Dale et al. 2009; Sheth et al. 2010; MacLachlan et al. 2011; Radburn-Smith et al. 2011; Sorce, Tully & Courtois 2012). The *Spitzer* Heritage Archive[3] provided direct online access to the science-ready frames.

(x) **UK 48-inch Schmidt telescope**
The UK 48-inch Schmidt, located at Siding Spring in Australia, was used in an all-sky survey. This was digitized into the DSS and was available science-ready through a virtual-observatory interface.

2.2 Astrometric calibration

The astrometric solution associated with the various observations would often be in disagreement between bands, causing galaxies to be offset slightly between bands. We therefore used the SOLVE-FIELD program, which is part of the astrometry.net project, to fit a new astrometric calibration to all the observations. The telescopes and cameras used in this study display great variety and consequently no single limiting magnitude in the bands can be given for our sample. In general, our photometry does not go as deep as the Comerón et al. (2011) study of edge-on galaxies, but our interest is in the brighter levels in order to constrain the light distributions for our modelling.

2.3 Masking

To avoid flux contamination, masking of all fore- and background objects was required. For each galaxy, the band with the most prominent stars was selected. We used the DS9 display tool to draw regions on each object, after which a custom PYTHON program set the pixels in these regions to a value of zero. Pixels with a value of zero are ignored by FITSKIRT and thus we do not need to interpolate over them. We also used this program to draw a polygon around each galaxy, beyond which the image was masked. In most cases there was only a little masking required. The galaxies closer to the galactic plane, however, required far more extensive masking, with the total number of masks drawn for ESO 274–G001 well beyond a thousand. The region masks were copied to the other bands using DS9. The files were then inspected and additional masking applied where required.

2.4 Normalization

To avoid overly long computations, all images were rotated to align their major axis with the horizontal image axis and then shrunk down to a width of ∼700 pixels. We subtract the average background from the image. The image was then divided by the total flux, such that the sum of the image became one. This last step is required by FITSKIRT, as it prevents a particularly bright band from dominating the fitting result.

3 DATA FITTING

The data will be modelled using FITSKIRT with the following components (de Geyter et al. 2013). The disc of each galaxy is modelled as a double-exponential disc. No truncation was included in the model, as this is currently not supported by FITSKIRT. Truncations are known to occur near the onset of the H I warp (van der Kruit 2007) and this region is not of interest for our goal of measuring the mid-plane hydrostatics (see also Section 2 of Paper III). Developing a truncated model was discussed, but, considering the quality of the data, the current research questions and the computational cost associated with additional free parameters, we have decided not to develop such an option. The disc thus follows the luminosity distribution

$$j(R,z) = \frac{L_{\mathrm{d},*}}{4\pi h_{R,*}^2 h_{z,*}} \exp\left(-\frac{R}{h_{R,*}}\right) \exp\left(-\frac{|z|}{h_{z,*}}\right), \quad (1)$$

with $L_{\mathrm{d},\star}$ the total disc luminosity, $h_{R,\star}$ and $h_{z,\star}$ the disc scalelength and scaleheight and R and z the radial and vertical coordinates.

The assumption of a double-exponential model in our fits is a simplification of reality. It is well-known that better fits are possible: van der Kruit (1988) proposed a sech-function as a compromise between the isothermal sech^2 distribution of van der Kruit & Searle (1981), which ignores the real situation that there are most likely age groups of stars with different velocity dispersions, and the mathematically convenient, but unphysical exponential. We believe our fits are sufficiently satisfactory that any further sophistication is not necessary; this is also in view of the fact that at low z, where the exponential and the sech deviate most, dust extinction would need to be fitted more realistically than the crude way we apply here, namely also with a double exponential. Also, the scaleheight of the stars may very well change with galactocentric distance, as found by de Grijs & Peletier (1997) and Narayan & Jog (2002). Again, our fits work very well with a constant scaleheight and we therefore believe these are adequate for our purposes. We return to this issue in section 5.2.

Our galaxies are close to edge-on and already van der Kruit & Searle (1981) have shown that small variations in inclination away from perfectly edge-on do not affect the scaleheight determined. Nevertheless, we leave the inclination in as a parameter (see below).

A bulge was also included, which follows the luminosity density (de Geyter et al. 2013)

$$j(R,z) = \frac{L_{\mathrm{b},*}}{q R_{\mathrm{e}}^3} S_{\mathrm{n}}\left(\frac{m}{R_{\mathrm{e}}}\right), \quad (2)$$

$$m = \sqrt{R^2 + \frac{z^2}{q^2}}, \quad (3)$$

with total bulge luminosity $L_{\mathrm{b},\star}$, effective radius R_{e}, Sérsic function

$$S_{\mathrm{n}} = I_{\mathrm{e}} \exp -C\left[\left(\frac{R}{R_{\mathrm{e}}}\right)^{1/n} - 1\right]$$

(with the proper normalization) and flattening of the bulge q. In general, our photometry is not deep enough to look for thick discs and what we fit as bulges may very well be the brighter parts of such components.

The dust is also modelled as a double-exponential disc

$$\rho_{\mathrm{d}}(R,z) = \frac{M_{\mathrm{d}}}{2\pi h_{R,\mathrm{d}}^2 h_{z,\mathrm{d}}} \exp\left(-\frac{R}{h_{R,\mathrm{d}}}\right) \exp\left(-\frac{|z|}{h_{z,\mathrm{d}}}\right), \quad (4)$$

with dust density ρ, total dust mass M_{d} and dust scalelength and scaleheight $h_{R,\mathrm{d}}$ and $h_{z,\mathrm{d}}$. The galaxies in our sample are late-type dwarfs and we do not expect them to have a lot of dust. We include dust in the results for completeness, but stress that we are skeptical about the exact quantities returned by the fitting. The inclination can vary between 86° and 90° to obtain the best fit. However, with the

[3] Available at http://sha.ipac.caltech.edu/applications/Spitzer/SHA/

absence of dust bands in most of our galaxies, we cannot confirm the exact inclination.

Including the inclination i and the exact central position, the model has a total of 11 global free parameters, plus two additional free parameters per band (the disc luminosity $L_{\mathrm{d},\star}$ and bulge-to-disc ratio B/D). FITSKIRT fits the data using the GALIB genetic algorithm (Wall 1996). We use a population of 200 individuals and evolve the model for 100 iterations. We run five fits for each galaxy. The Millipede Cluster of the University of Groningen was used to perform all fits. A fit typically takes 30 h.

Due to the random path that the light follows in the model, no two instances of the model will be the same. As such, both the observation and the model contain Poisson-distributed noise. The objective function to measure the error is therefore

$$\chi^2 = \sum_j^{N_{\mathrm{pix}}} \frac{(I_{\mathrm{mod},j} - I_{\mathrm{obj},j})^2}{\sigma^2} = \sum_j^{N_{\mathrm{pix}}} \frac{(I_{\mathrm{mod},j} - I_{\mathrm{obj},j})^2}{|I_{\mathrm{obj},j}| + I_{\mathrm{mod},j}}. \quad (5)$$

The lowest χ^2 value is adopted as the true value. The error in each parameter is taken as the standard deviation from the five runs.

4 RESULTS

The results for each galaxy are shown in Table 1. The quality of the individual fits can be seen in Table A2 in the online Appendix. When available, we also list the published integrated magnitude $L_{\mathrm{band},\star}$. Where needed, these have been corrected for Galactic foreground extinction using the Schlafly & Finkbeiner (2011) re-calibration of the Schlegel, Finkbeiner & Davis (1998) infrared-based dust map, as calculated in NED. Before the disc luminosity $L_{\mathrm{d},\star}$ produced in FITSKIRT can be used for further analysis, it first needs to be calibrated. This can be done by multiplying it by $10^{15} L_{\mathrm{band},\star}$, where $L_{\mathrm{band},\star}$ is the integrated luminosity, expressed in W m^{-2}, as measured without dust absorption.

4.1 IC 2531

Galaxy IC 2531 (see Fig. 1) is the only Sb galaxy in our sample and has the highest maximum circular velocity at $v_{\mathrm{max}} = 260.5$ km s^{-1} (Table 1). This is nearly twice the maximum circular velocity of the other galaxies in our sample. The central brightness component has not been reproduced correctly. This bulge is most likely peanut-shaped or boxy, which requires a different bulge model from that adopted here (Jarvis 1986; de Souza & Dos Anjos 1987). The scalelength is $h_{R,*} = 5077 \pm 262$ pc and the scaleheight $h_{z,*} = 613 \pm 46$ pc. Kregel et al. (2002a) report a much longer $h_{R,*} = 12511 \pm 2643$ pc and $h_{z,*} = 658.5 \pm 65.8$ pc. The galaxy features a very prominent dust lane, which the Kregels *I*-band model does not treat for, and so their scalelength might be overestimated. Xilouris et al. (1999) have also performed a fit to the galaxy that did include a treatment for dust. They report a *K*-band scalelength of $h_{R,*} = 5.04 \pm 0.1$ kpc and a scaleheight of 0.45 ± 0.02 kpc. The dust is found to have a (*K*-band) scalelength of $h_{\mathrm{R,d}} = 8.00 \pm 0.3$ kpc and a scaleheight of $h_{\mathrm{z,d}} = 0.22 \pm 0.03$ kpc, which is similar to the $h_{\mathrm{R,d}} = 7.0 \pm 2.2$ kpc and $h_{\mathrm{z,d}} = 0.3 \pm 0.1$ kpc reported here.

4.2 IC 5052

Galaxy IC 5052 has proven hard to model, as the galaxy showed clear asymmetries. We therefore opted to model both sides of the galaxy separately (Figs 2, 3, 4 and 5). This forced us to fix the centre of the galaxy, which has clearly hampered the results. From an inspection of the images, we conclude that the left side represents the galaxy better, although the fit is far from perfect. The scalelength for the left side, $h_{R,*}$, is 857 ± 68 pc and the scaleheight, $h_{z,*}$, is 124 ± 80 pc, which makes this the galaxy with the shortest scalelength in our sample. Comerón et al. (2011) have also modelled this galaxy using a double-disc approach and report a thick-disc scalelength of 470–530 pc and a thin-disc scalelength of 140–170 pc. They note that the galaxy can also be modelled successfully with a single disc. Overall, we find that the galaxy is very clumpy in its light distribution, which cannot be fitted properly by the models. Our fitted scalelength differs considerably between the two sides and both values are much larger than the one determined by Comerón et al. (2011). Our result should be treated with much caution. This galaxy has proved to be too difficult to model for our purposes and it has been deleted from our sample in Paper V, where we perform the final analysis.

4.3 IC 5249

The overall quality of the fit is very good (see Figs 6 and 7). The scalelength is $h_{R,*} = 6828 \pm 340$ pc, while the scaleheight is $h_{z,*} = 242 \pm 20$ pc. Similar results have also been found in previous studies. Carignan (1983) analysed the galaxy in the *B* band and distinguished two components with scalelengths 18 and 2.5 kpc. Wainscoat (1986) confirmed these results using *H*-, *I*- and *K*-band data. The galaxy was also analysed by Byun (1992) in the *B*, *R* and *I* bands (van der Kruit et al. 2001). Abe et al. (1999) discovered a very sharp truncation at two scalelengths. We do not find any indication

Table 1. The global properties of the stellar fits per galaxy. QOF is the quality of the fit: good, moderate or bad.

Name	Stellar scalelength [pc]	Stellar scaleheight [pc]	Dust scalelength [pc]	Dust scaleheight [pc]	Dust mass [10^7 M$_\odot$]	Bulge radius [pc]	Bulge flattening	Inclination °	Sérsic Index	QOF
IC 2531	5077 ± 262	613 ± 46	6997 ± 2213	311 ± 109	4 ± 1.3	5451 ± 1775	0.78 ± 0.22	88.7 ± 0.8	5.6 ± 1.0	G
IC 5052 (left)	857 ± 68	124 ± 80	1500 ± 3655	600 ± 15	0.5 ± 0.44	1600 ± 518	0.25 ± 0.02	86.0 ± 1.7	0.5 ± 0.2	M
IC 5052 (right)	1617 ± 129	781 ± 299	6664 ± 2042	523 ± 96	0.01 ± 0.5	2149 ± 45	0.16 ± 0.05	87.7 ± 1.0	0.5 ± 0.0	B
IC 5249	6828 ± 340	242 ± 20	4380 ± 677	372 ± 67	0.88 ± 0.2	4602 ± 183	0.22 ± 0.01	88.8 ± 0.9	2.9 ± 0.2	G
ESO 115–G021	1108 ± 280	149 ± 101	10515 ± 2057	432 ± 69	2.4 ± 0.47	3810 ± 1159	0.35 ± 0.06	86.0 ± 0.7	2.6 ± 0.7	G
ESO 138–G014	2288 ± 59	217 ± 10	3074 ± 508	509 ± 34	1.5 ± 0.23	5843 ± 611	0.18 ± 0.01	86.8 ± 0.3	3.7 ± 0.3	G
ESO 146–G014	5356 ± 1384	1000 ± 422	7115 ± 1063	525 ± 58	2.3 ± 0.47	3264 ± 1356	0.09 ± 0.10	86.0 ± 0.0	0.9 ± 0.3	G
ESO 274–G001	1270 ± 59	161 ± 2	11374 ± 373	472 ± 33	2.9 ± 0.69	4880 ± 551	0.06 ± 0.02	86.8 ± 0.2	0.6 ± 0.1	G
UGC 7321	2498 ± 349	187 ± 80	8568 ± 1956	600 ± 139	6.2 ± 1.1	2532 ± 1013	0.10 ± 0.02	90.0 ± 1.1	1.9 ± 0.7	G

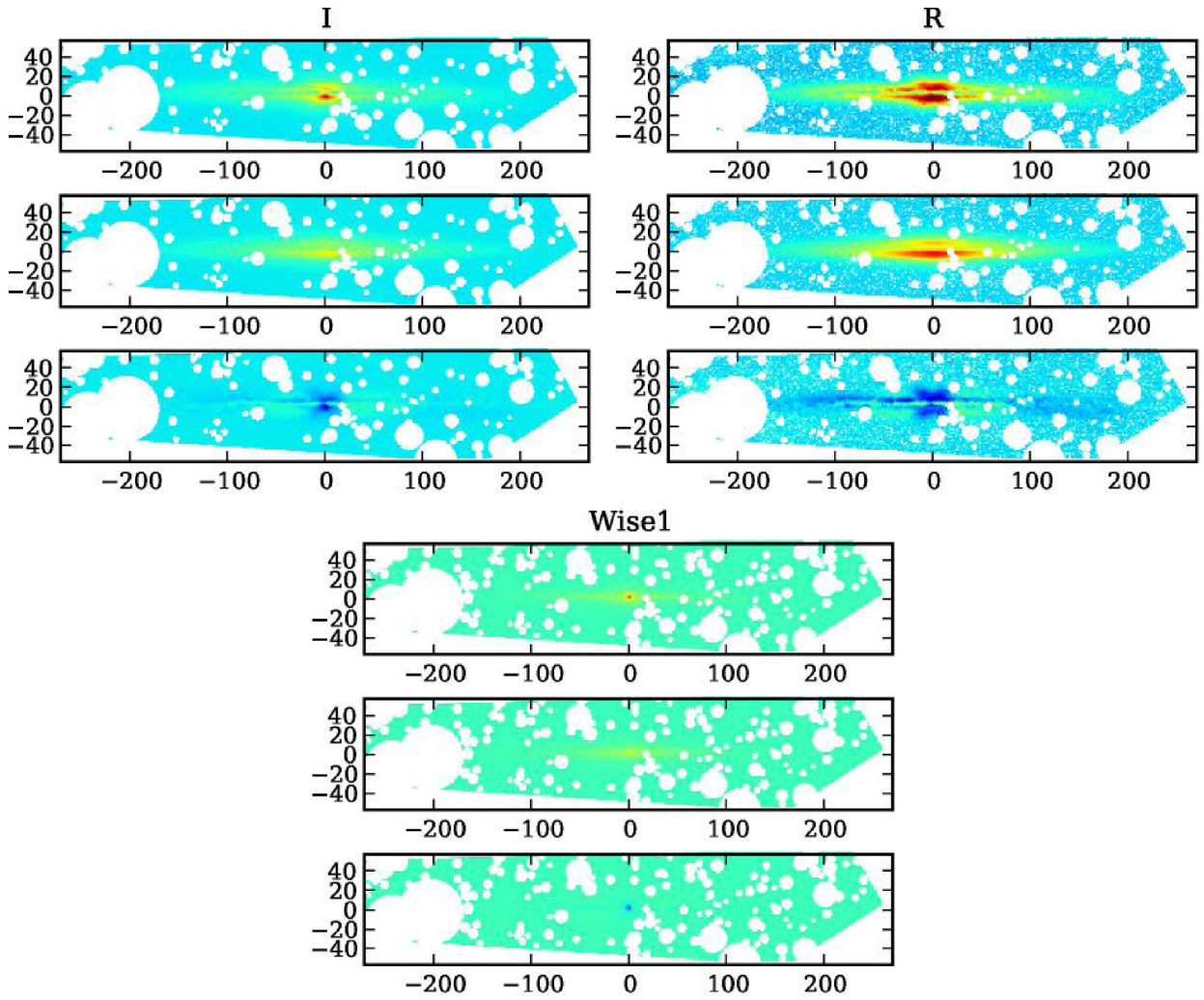

Figure 1. Stellar decompositions for IC 2531. Each band consists of three panels. The top panels show the observation, the middle panels the best-fitting models and the lower panels the difference maps. Colour scaling is equal between the three panels. The scale of the images is in arcsec.

of a second disc component as Carignan (1983) did, although their second component might well have been the bulge we find here. This galaxy is an example of a so-called superthin galaxy. van der Kruit et al. (2001), who found a scalelength of about 7 kpc, attributed this to the relatively long scalelength combined with the low (face-on) surface brightness.

4.4 ESO 115–G021

A large amount of masking was required for ESO 115–G021 (Fig. 8). The dwarf galaxy has been modelled successfully, although it is still clumpy. The stellar disc scalelength $h_{R,*}$ is only 1108 ± 280 pc, while the scaleheight $h_{z,*}$ is only 149 pc. The galaxy is very faint and emits only 5.0×10^7 $L_\odot$ in the R band. In comparison with the neutral hydrogen mass, $M_{\rm HI}/L_{\rm R}$ is 12.5, the highest value in our sample.

4.5 ESO 138–G014

ESO 138–G014 also required extensive masking (Fig. 9). Despite this, the overall fit is good. With $h_{R,*} = 2288 \pm 59$ pc and $h_{z,*} = 217 \pm 10$ pc, the stellar disc is twice as long as in ESO 115–G021 and slightly thicker. Kregel et al. (2002a) previously modelled this galaxy without dust and reported a larger disc with $h_{R,*} = 3779$ pc and $h_{z,*} = 382 \pm 10$ pc.

4.6 ESO 146–G014

ESO 146–G014 is a known low-surface-brightness galaxy and is extremely metal-poor (Roennback & Bergvall 1995; Morales-Luis et al. 2011). The galaxy is a slow rotator ($v_{\rm max} = 84.1$ km s^{-1}) and is very patchy in nature, as can be seen in Fig. 10. Because of this, the fit is far from perfect. As can be seen in all three bands, the galaxy has a very bright central region, but also has a bright spot 50 arcsec east of the centre. The galaxy is also asymmetric, as can be seen most clearly in the V-band image.

4.7 ESO 274–G001

Galaxy ESO 274–G001 is very close to the Galactic plane, with a Galactic latitude of only 9.3°. The four bands therefore required an exceptional amount of masking (Fig. 11), but the fit was still successful. The galaxy has a stellar disc scalelength $h_{R,*}$ of 1270 ± 59 pc and a scaleheight $h_{z,*}$ of 161 ± 2 pc, which is very similar

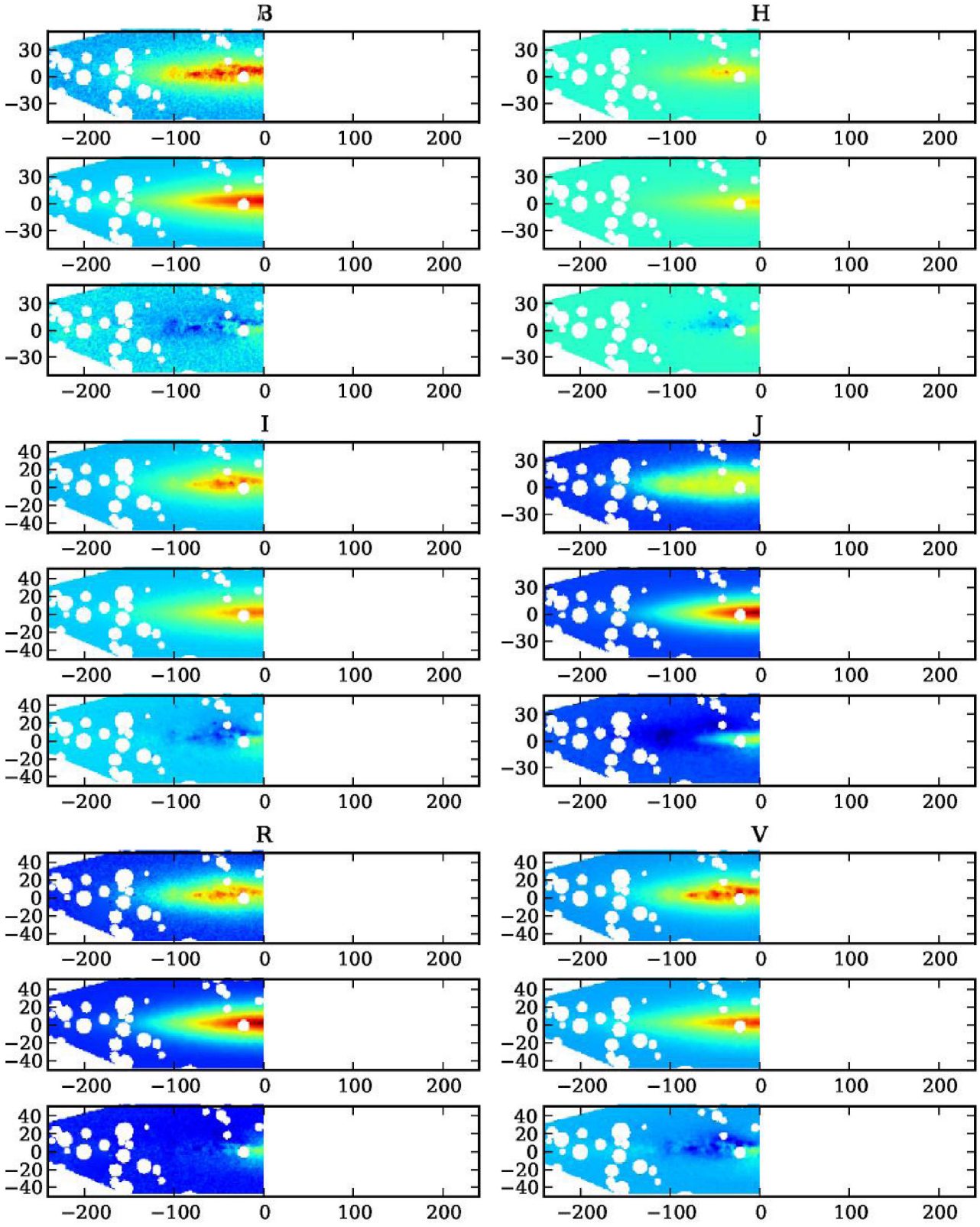

Figure 2. Stellar decompositions for the left side of IC 5052 (1/2). Each band consists of three panels. The top panels show the observation, the middle panels the best-fitting models and the lower panels the difference maps. Colour scaling is equal between the three panels. The scale of the images is in arcsec.

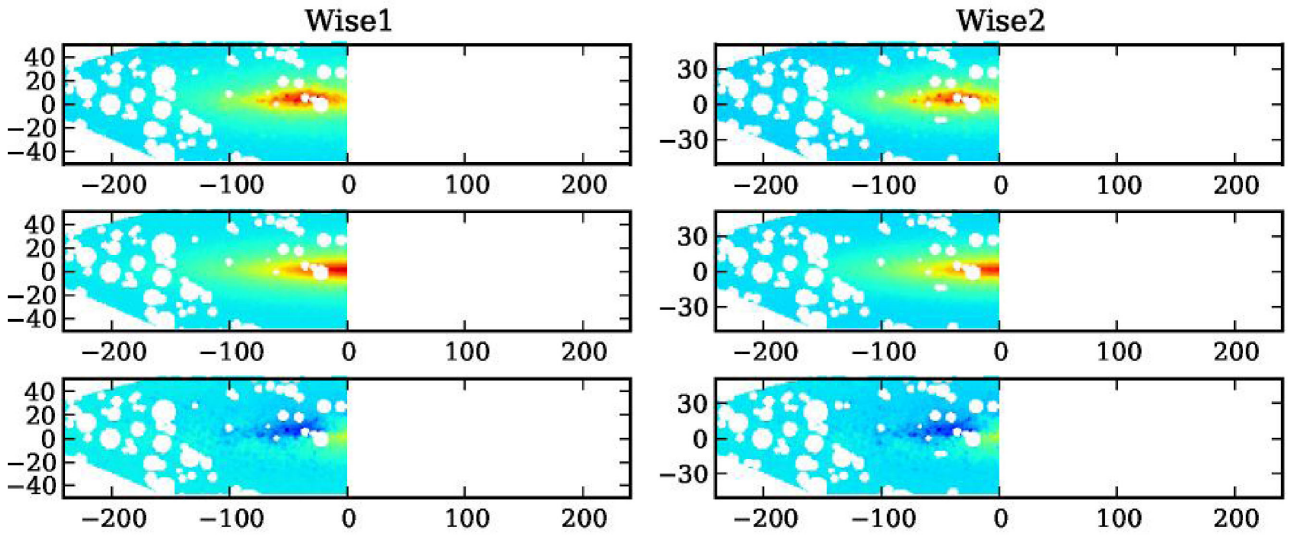

Figure 3. Stellar decompositions for the left side of IC 5052 (2/2). Each band consists of three panels. The top panels show the observation, the middle panels the best-fitting models and the lower panels the difference maps. Colour scaling is equal between the three panels. The scale of the images is in arcsec.

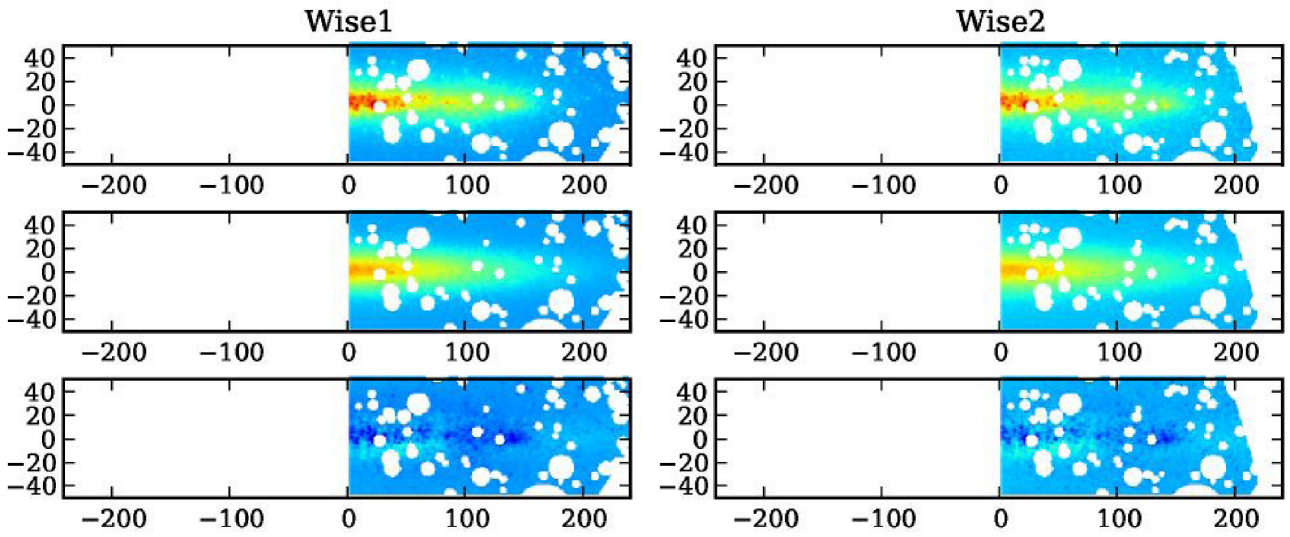

Figure 4. Stellar decompositions for the right side of IC 5052 (1/2). Each band consists of three panels. The top panels show the observation, the middle panels the best-fitting models and the lower panels the difference maps. Colour scaling is equal between the three panels. The scale of the images is in arcsec.

to ESO 115–G021. The overall appearance is different from that galaxy, as ESO 274–G001 has a far more flattened bulge. Similarly to ESO 115–G021 and ESO 146–G014, the galaxy is a slow rotator, with a maximum circular velocity of $v_{\rm max} = 103.9$ km s^{-1}. Moreover, similarly to those two galaxies, ESO 274–G001 is patchy in nature. The galaxy has the highest luminosity compared with its optically thin H I mass: $M_{\rm HI}/L_{\rm R} = 0.8$.

4.8 UGC 7321

UGC 7321 has been modelled using five bands (Fig. 12), the results of which have the lowest combined χ^2 error in this sample. The scalelength has been measured at $h_{R,*} = 2498 \pm 349$ pc and the scaleheight at $h_{z,*} = 187 \pm 80$ pc. This is in agreement with O'Brien et al. (2010), who applied the deprojection method and reported $h_{\rm d,*} = 2650$ pc and $h_{z,*} = 245$ pc. The scaleheight was reported as 140–150 pc by Matthews, Gallagher & van Driel (1999), who did not discern a bulge. We emphasize that our fitted bulge may also correspond to the brighter parts of a thick disc.

O'Brien et al. (2010) performed a rotation-curve decomposition on the galaxy and found a mass-to-light $M_*/L_{r'}$ upper limit of 1.05. This implies a recent burst of star formation in the galaxy, which matches the detection of a significant fraction of young stars in the disc (Matthews et al. 1999). O'Brien et al. (2010) also performed a fit to the vertical hydrostatics of the disc and found a good fit at M_*/L_R of 0.2.

5 DISCUSSION

5.1 Quality of the fits

What can we conclude about the overall quality of the fits? In comparison with the available literature, we see that IC 2531, IC 5249 and UGC 7321 are in agreement with the results by others. The

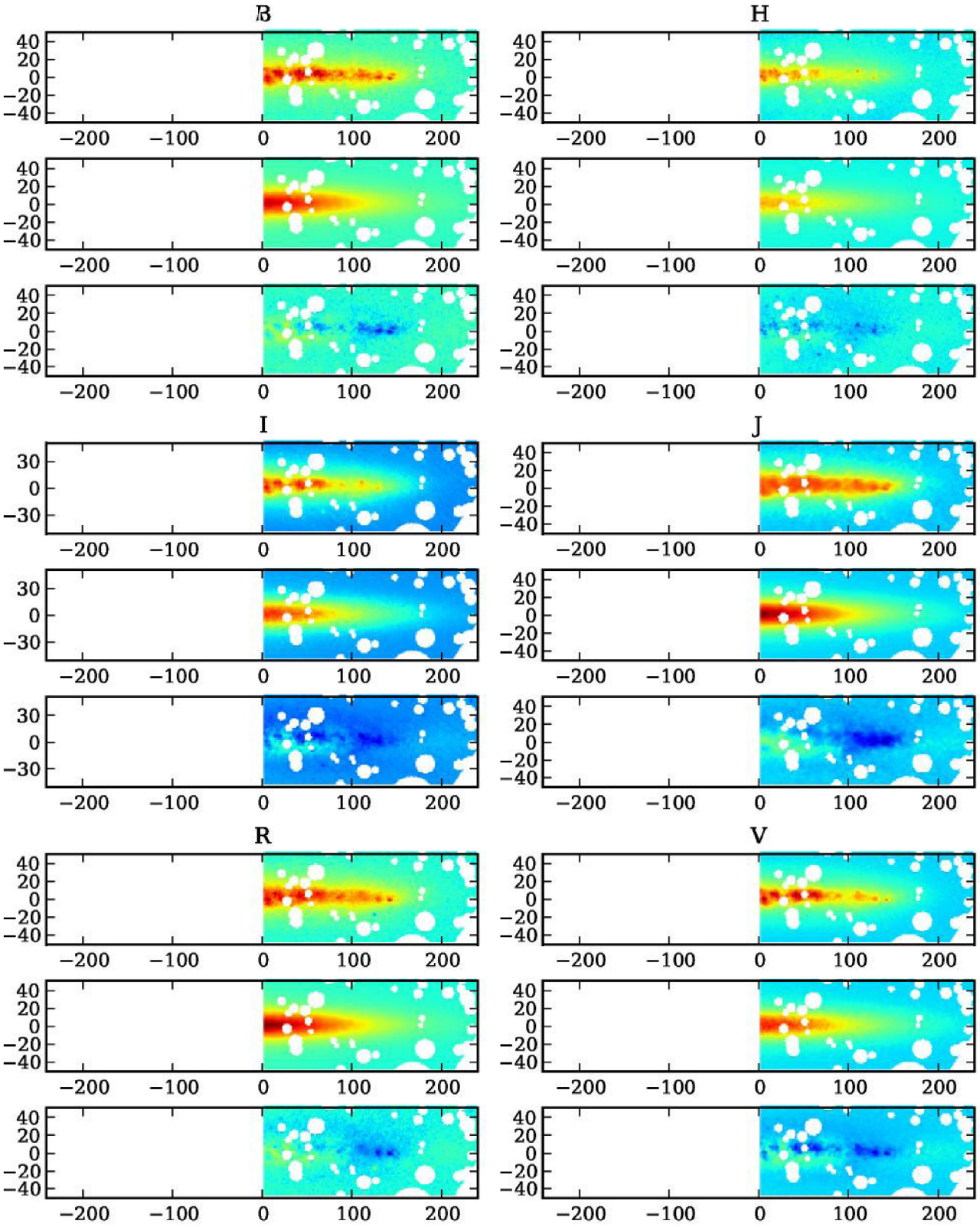

Figure 5. Stellar decompositions for the right side of IC 5052 (2/2). Each band consists of three panels. The top panels always show the observation, the middle panels the best-fitting models and the lower panels the difference maps. Colour scaling is equal between the three panels. The scale of the images is in arcsec.

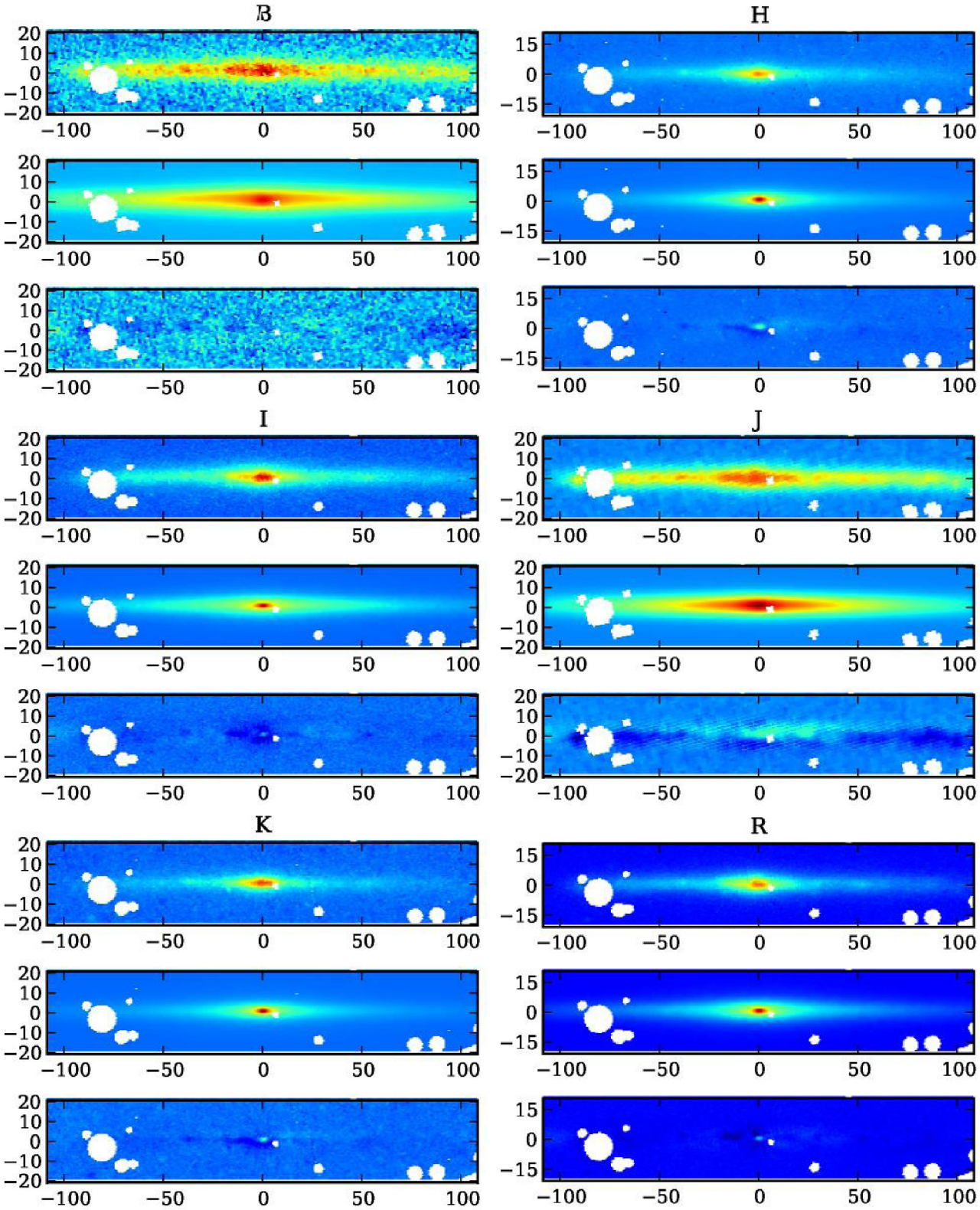

Figure 6. Stellar decompositions for IC 5249 (1/2). Each band consists of three panels. The top panels always show the observation, the middle panels the best-fitting models and the lower panels the difference maps. Colour scaling is equal between the three panels. The scale of the images is in arcsec.

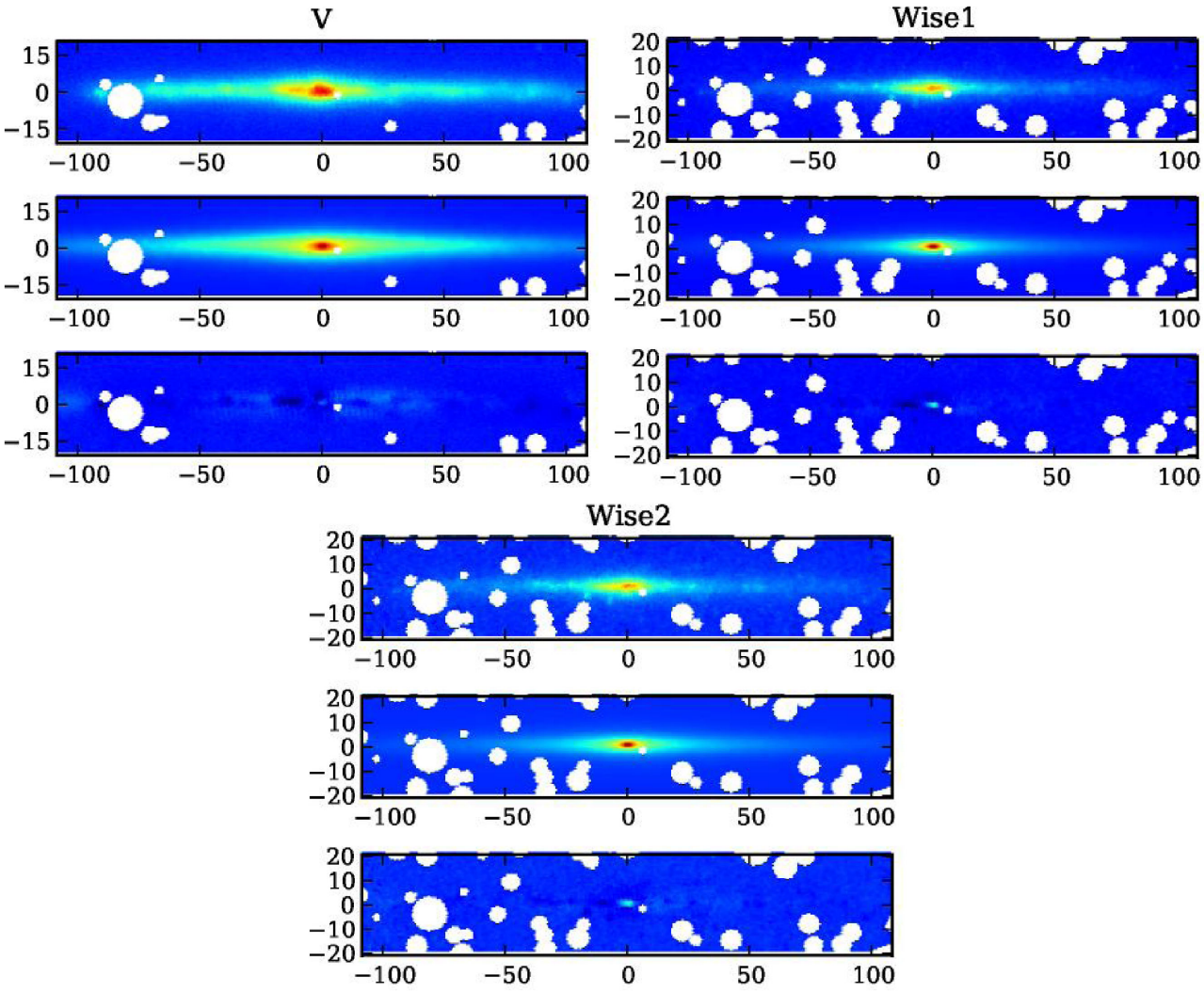

Figure 7. Stellar decompositions for IC 5249 (2/2). Each band consists of three panels. The top panels always show the observation, the middle panels the best-fitting models and the lower panels the difference maps. Colour scaling is equal between the three panels. The scale of the images is in arcsec.

more slowly rotating galaxies, e.g. ESO 115–G021, ESO 146–G014 and ESO 274–G001, all have a clumpy nature, which makes fitting harder. For IC 5052 and ESO 138–G014, the parameters reported by other authors are different. As we noted before, IC 5052 gave us problems in modelling, so our results could well be wrong. ESO 138–G014 also required extensive masking. It is a low-surface-brightness galaxy, but the fit we have performed still looks acceptable (see Fig. 9). As such, we feel that the derived stellar disc scalelengths and scaleheights are reasonably accurate, with the possible exception of IC 5052.

A similar endeavor to the work carried out in this article was previously undertaken by de Geyter et al. (2014), who set out to model edge-on galaxies in CALIFA, which showed a clear dust band. In total they settled on a sample of 12 – mostly early-type – galaxies, for which they performed an oligochromatic fit to the g', r', i' and z' bands. While their data are of higher quality, their results are very similar to ours and they 'conclude that in general most galaxies are modelled accurately, especially when keeping in mind that the FITSKIRT models only consist of three basic components and they were determined by an automated procedure over a large parameters space without strong initial boundary conditions' (de Geyter et al. 2014).

5.2 On the z distribution

A key assumption in our model is the use of a double-exponential disc (see equation 1). This choice was made as a basis for the hydrostatic equilibrium calculations in Paper V. Other functional forms for the vertical distribution were available, but were rejected as the quality of the observations does not allow us to distinguish accurately enough between the various forms.

To demonstrate this, we have presented the vertical distribution of UGC 7321 along a slice of the galaxy in Fig. 13. UGC 7321 was one of our most succesful fits, and as such the profiles between the model and the observation match sufficiently well. Even in this slice, however, there is a difference in the quality of the fit. The Wise2 fit has been very well reproduced, yet the R-band profile has been reproduced considerably less well, showing excess light further above and beyond the plane. The fits are influenced by the fact that the program tries to compensate for the local structures and contaminations (e.g. stray light due to field stars). More accurate and less contaminated observations are required to test accurately which functional form of the vertical distribution works best.

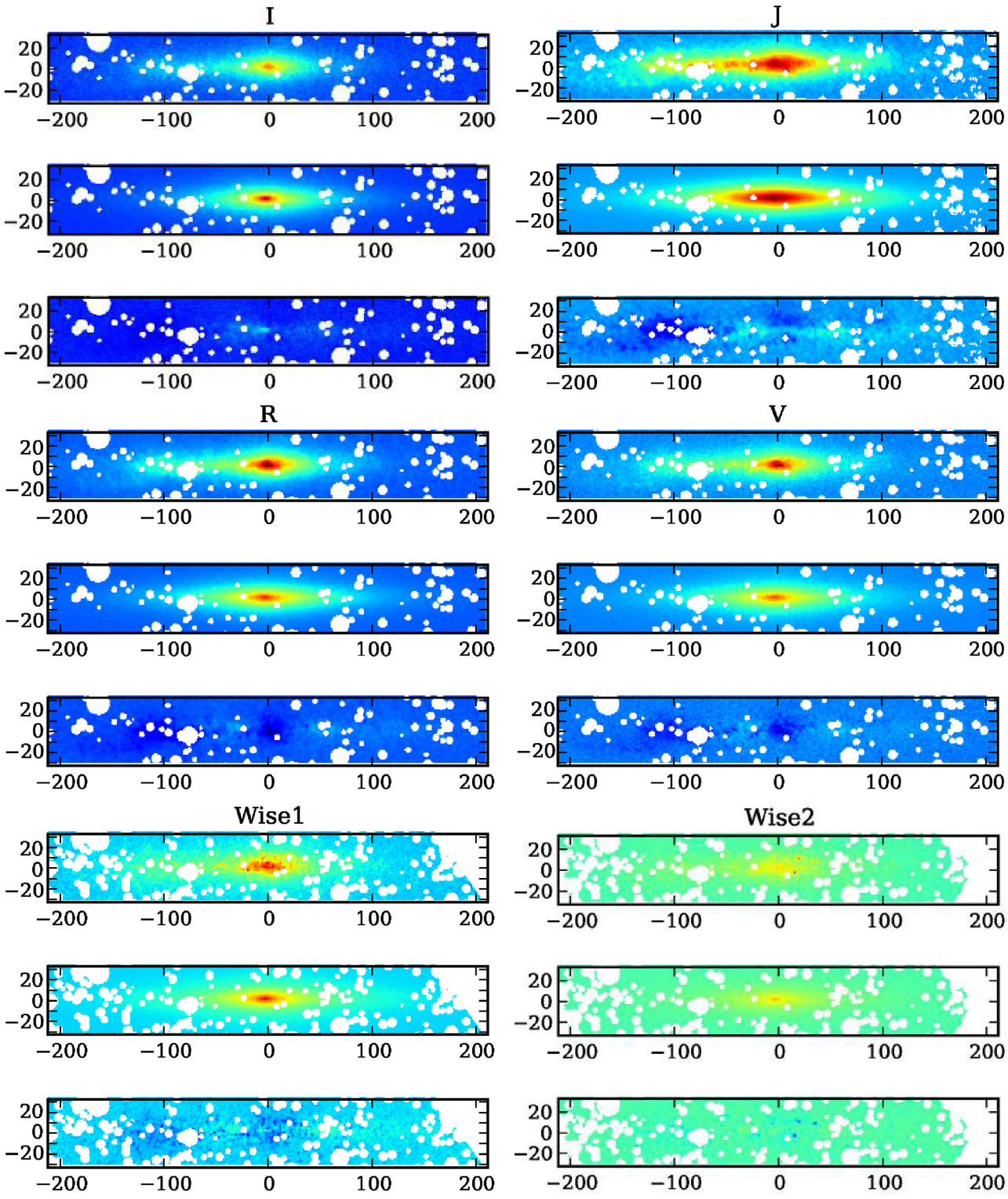

Figure 8. Stellar decompositions for ESO 115–G021. Each band consists of three panels. The top panels always show the observation, the middle panels the best-fitting models and the lower panels the difference maps. Colour scaling is equal between the three panels. The scale of the images is in arcsec.

5.3 Discs and bulges

Let us now compare the global properties of the stellar discs. Focusing on the seven good fits, the average stellar disc scalelength in our sample is $h_{R,*} = 3.49 \pm 2.24$ kpc, while the average scaleheight of the stellar disc is $h_{z,*} = 0.37 \pm 0.32$ kpc. As a comparison, de Geyter et al. (2014) report 4.23 ± 1.23 kpc and 0.51 ± 0.27 kpc for their 12 edge-ons sample. They also calculate the mean values for the 34 edge-on galaxies in Kregel, van der Kruit & de Grijs (2002b), reporting 4.73 ± 2.57 kpc and 0.57 ± 0.25 kpc. That sample consists of Sa-, Sb- and Sc-type galaxies, while ours consists mostly of

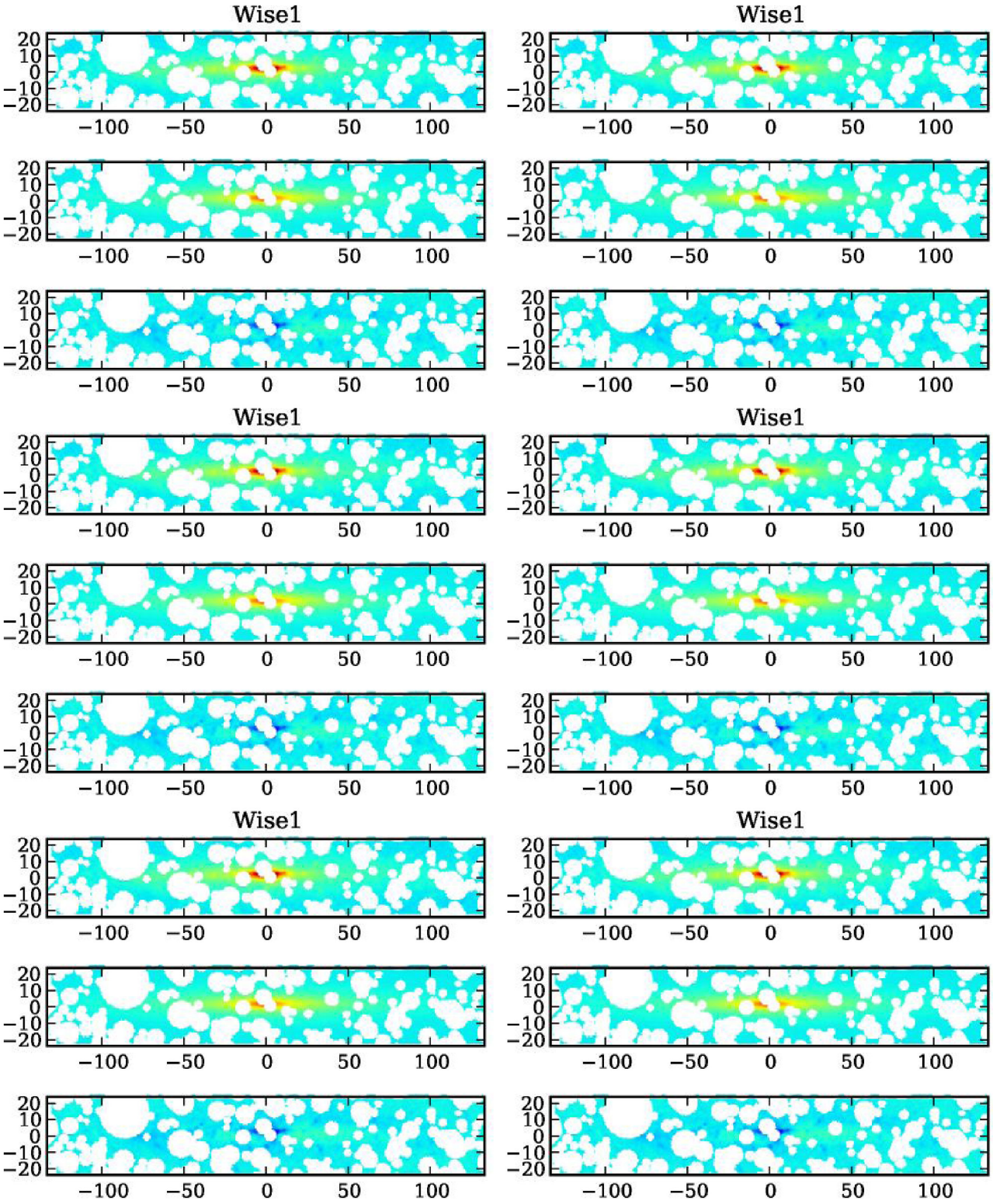

Figure 9. Stellar decompositions for ESO 138–G014. Each band consists of three panels. The top panels always show the observation, the middle panels the best-fitting models and the lower panels the difference maps. Colour scaling is equal between the three panels. The scale of the images is in arcsec.

Sd-type galaxies (table 2 of Paper I of this series). IC 5249 appears to be a unique galaxy in terms of scalelength to scaleheight ratio. If we remove it from the sample, the averages become even more distinct, with $h_{R,*} = 2.93 \pm 1.85$ kpc and $h_{z,*} = 0.38 \pm 0.28$ kpc. It is typically not expected that the scalelengths for disc galaxies depend on Hubble morphological types between Sa and Sc (de Jong 1996; Graham & de Blok 2001). However, for Scd and Sd galaxies, it was demonstrated using face-on galaxies that the scalelength tends to be significantly shorter (Fathi et al. 2010) and our results are within expectations: although the range we find is large,

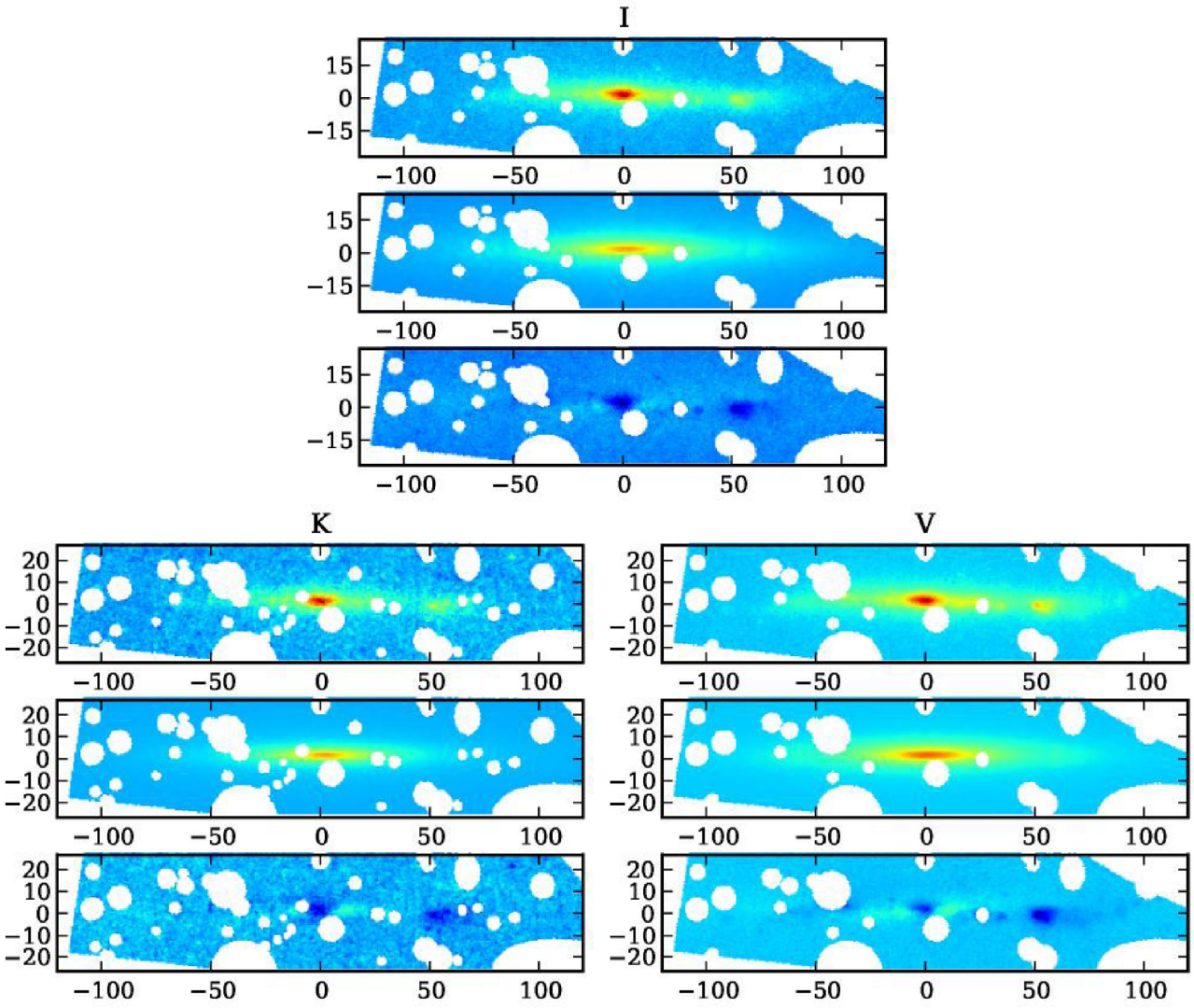

Figure 10. Stellar decompositions for ESO 146–G014. Each band consists of three panels. The top panels always show the observation, the middle panels the best-fitting models and the lower panels the difference maps. Colour scaling is equal between the three panels. The scale of the images is in arcsec.

the mean is still less than the values we just quoted for Sa to Sc galaxies.

If we now focus on the scalelength over scaleheight ratio, we find an average of $h_{R,*}/h_{z,*} = 11.6 \pm 7.76$. IC 5249 has by far the highest value at 28.2, which makes it a 'superthin' disc. Removing this one galaxy, the average ratio becomes $h_{R,*}/h_{z,*} = 8.81 \pm 2.78$. A very similar value of $h_{R,*}/h_{z,*} = 8.26 \pm 3.44$ was reported by de Geyter et al. (2014) for their own sample and a value of $h_{R,*}/h_{z,*} = 8.21 \pm 2.36$ for the Kregel et al. (2002b) sample. We conclude that our measurements are, with the possible exception of IC 5249, in good agreement with their samples.

Looking at the bulges, we find a typical bulge effective radius of $R_e = 4.34 \pm 1.19$ kpc. This is longer than reported by de Geyter et al. (2014), who report the value of $R_e = 2.31 \pm 1.59$ kpc. This was already large compared with the 1000-galaxy sample of Gadotti (2009), who reported $R_e = 0.84 \pm 0.36$ kpc. It was argued by de Geyter et al. (2014) that this difference is due to the lack of dust attenuation correction in Gadotti (2009) and the lack of a treatment of bars in their own work. The Gadotti (2009) sample does not contain many Sd galaxies; there might be different averages that apply for an Sd sample. However, given our results from the previous section, we argue that it is more likely that our bulges are not fitted very reliably. The average Sérsic index we find is 2.6 ± 1.7, which is consistent with the value of 2.37 ± 1.35 reported by de Geyter et al. (2014). As we pointed out above, there is a real possibility that our bulge components really are the brighter parts of a thick disc.

5.4 Dust

Most of the galaxies in our sample are slow rotators. The Sd-type galaxies have a maximum circular rotation of $v_{max} = 131.9$ km s^{-1}. Only IC 2531 has a much higher rotation of $v_{max} = 260.5$ km s^{-1} (table 4 of Paper I). Dalcanton, Yoachim & Bernstein (2004) found that, for galaxies rotating with a lower circular velocity than $v_{max} \sim 120$ km s^{-1}, no dust lane forms. Instead, the dust settles in more a clumpy structure. Inspecting the images of the galaxies, we can confirm this distinction in our own sample as well, although it is hard to distinguish for those discs just above 120 km s^{-1}. The average dust scalelength and scaleheight are $h_{R,\,d} = 4.34 \pm 1.19$ kpc and

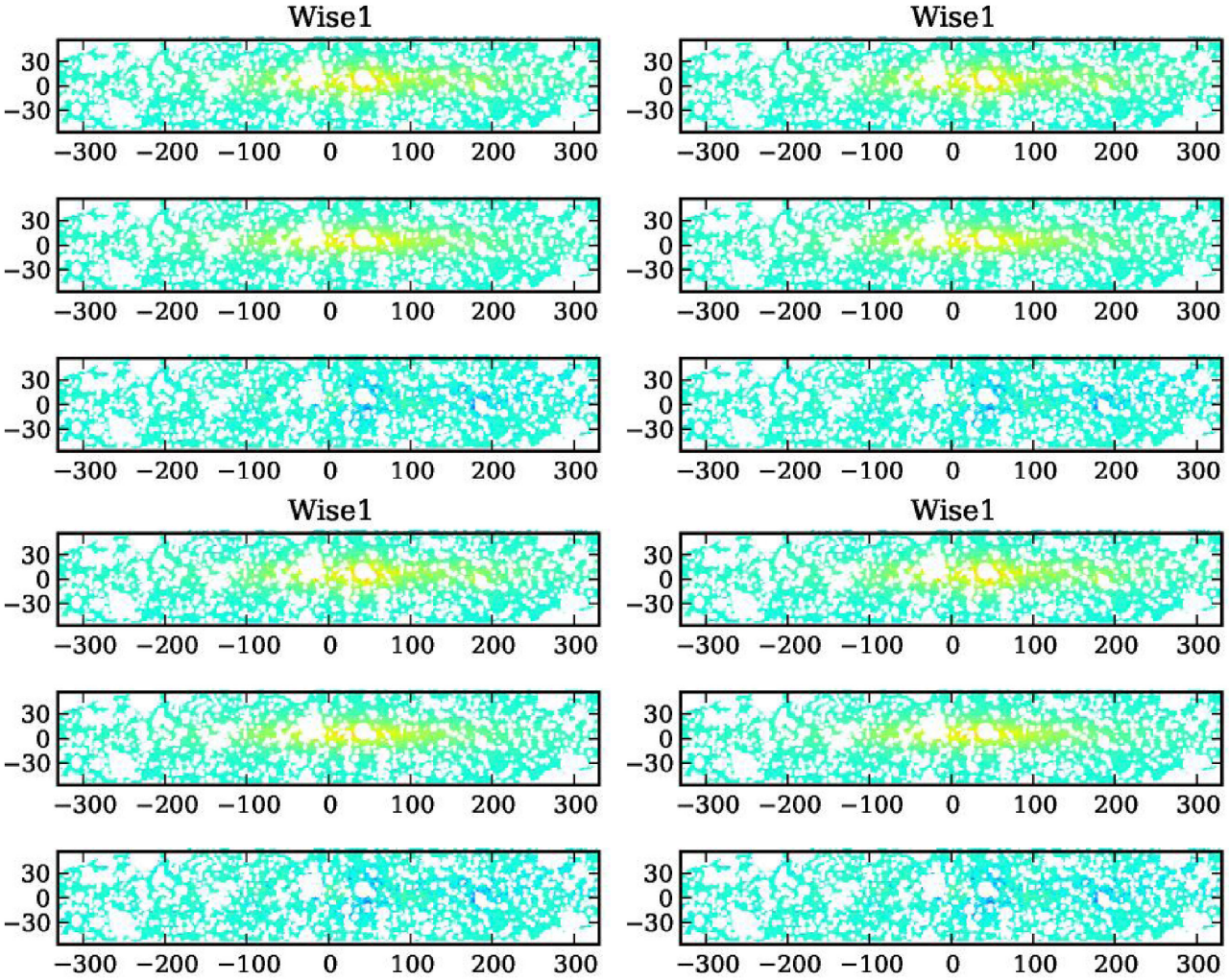

Figure 11. Stellar decompositions for ESO 274–G001. Each band consists of three panels. The top panels always show the observation, the middle panels the best-fitting models and the lower panels the difference maps. Colour scaling is equal between the three panels. The scale of the images is in arcsec.

$h_{z,\mathrm{d}} = 0.46 \pm 0.01$ kpc, while the ratio between the two is on average $h_{R,\mathrm{d}}/h_{z,\mathrm{d}} = 10.1 \pm 4.4$. A typical dust scalelength and height of $h_{R,\mathrm{d}} = 6.03 \pm 2.92$ and $h_{z,\mathrm{d}} = 0.23 \pm 0.10$ was reported by de Geyter et al. (2014). For the scaleheight, similar values of $h_{z,\mathrm{d}} = 0.23 \pm 0.08$ kpc and $h_{z,\mathrm{d}} = 0.25 \pm 0.11$ were reported by Xilouris et al. (1999) and Bianchi (2007). Our galaxies thus typically have a thicker dust layer than the samples of these authors.

Dalcanton et al. (2004) argued that, for discs rotating more slowly than a circular velocity of $v_{\mathrm{max}} \sim 120$ km s^{-1}, the dust would follow a thicker distribution than the faster rotating sample. Indeed, most of our galaxies are below or near a circular velocity of 120 km s^{-1}. Taking the three galaxies with circular velocities above 130 km s^{-1}, we have an average scalelength to scaleheight ratio of $h_{R,\mathrm{d}}/h_{z,\mathrm{d}} = 13.8 \pm 3.3$, compared with $h_{R,\mathrm{d}}/h_{z,\mathrm{d}} = 7.4 \pm 2.7$ for the other four. The sample of de Geyter et al. (2014) has a mean ratio of $h_{R,\mathrm{d}}/h_{z,\mathrm{d}} = 26.2$, which is much closer to our fast-rotating galaxy at $h_{R,\mathrm{d}}/h_{z,\mathrm{d}} = 17.5$.

However, UGC 7321 with a maximum circular velocity of $v_{\mathrm{max}} = 128$ km s^{-1} has a very different ratio of $h_{R,\mathrm{d}}/h_{z,\mathrm{d}} = 4.2$. This galaxy also has the greatest dust mass of the sample, 6.2×10^7 M$_\odot$, compared with the average of $2.8 \pm 1.82 \times 10^7$ M$_\odot$ for the entire sample. There is no distinction in terms of dust mass to be made between slow and fast rotators.

The dust scalelength to stellar scalelength ratio is on average $h_{R,\mathrm{d}}/h_{R,*} = 1.88 \pm 1.37$ in our sample. This is compatible with the value $h_{R,\mathrm{d}}/h_{R,*} = 1.73 \pm 0.83$ reported by de Geyter et al. (2014). Xilouris et al. (1999) report $h_{R,\mathrm{d}}/h_{R,*} = 1.36 \pm 0.17$ and Bianchi (2007) find $h_{R,\mathrm{d}}/h_{R,*} = 1.53 \pm 0.55$; both values are compatible with ours. The dust scaleheight to stellar scaleheight ratio we report is $h_{z,\mathrm{d}}/h_{z,*} = 1.99 \pm 1.15$. Although compatible, this is much higher than the value of $h_{z,\mathrm{d}}/h_{z,*} = 0.55 \pm 0.22$ reported by de Geyter et al. (2014), the value of $h_{z,\mathrm{d}}/h_{z,*} = 0.58 \pm 0.13$ reported by Xilouris et al. (1999) and the value of $h_{z,\mathrm{d}}/h_{z,*} = 0.52 \pm 0.49$ reported by Bianchi (2007). We thus find that the dust to stellar scalelength ratio of our late-type galaxies sample is compatible with more early-type samples; the dust to stellar scaleheight ratio is far higher. The dust in our slow-rotating galaxies sample forms into a much thicker disc, as predicted by Dalcanton et al. (2004).

6 CONCLUSIONS

In this article, we have attempted to fit the bulge and disc of eight edge-on dwarf galaxies using FITSKIRT automatically. The quality of our fit varies, mostly due to the limited quality of the available data and the intrinsic low luminosity of these galaxies. Despite this, we have successfully recovered the stellar discs in seven out of

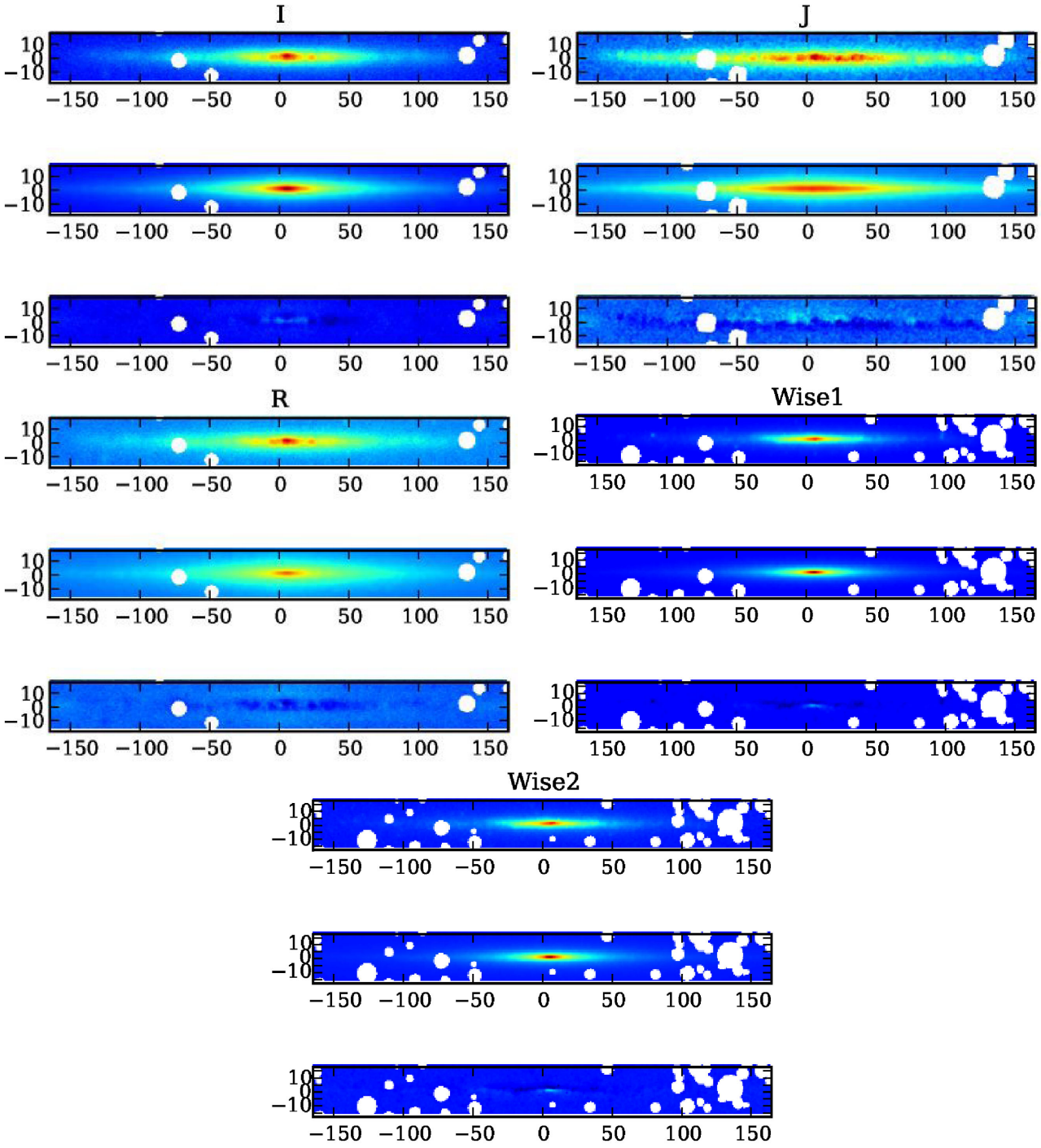

Figure 12. Stellar decompositions for UGC 7321. Each band consists of three panels. The top panels always show the observation, the middle panels the best-fitting models and the lower panels the difference maps. Colour scaling is equal between the three panels. The scale of the images is in arcsec.

eight of the galaxies in our sample. The results for the bulges are less reliable, most likely due to the lack of an accurate description for bars in the code. We have also measured the dust distribution in these seven galaxies successfully. The average dust scalelength to stellar scalelength is compatible with other samples, but our dust scaleheight to stellar scaleheight ratio is far higher than in other typical samples. The H I mass-to-light ratio $M_{\rm H\,I}/L_R$ varies drastically between the various galaxies. It is only 0.2 in ESO 274–G001, yet 12.5 in ESO 115–G021.

ACKNOWLEDGEMENTS

SPCP is grateful to the Space Telescope Science Institute, Baltimore, USA, the Research School for Astronomy and Astrophysics, Australian National University, Canberra, Australia, and the Instituto de Astrofisica de Canarias, La Laguna, Tenerife, Spain, for hospitality and support during short and extended working visits in the course of his PhD thesis research. He thanks Roelof de Jong and Ron Allen for help and support during an earlier period as a visiting student at Johns Hopkins University and the Physics and

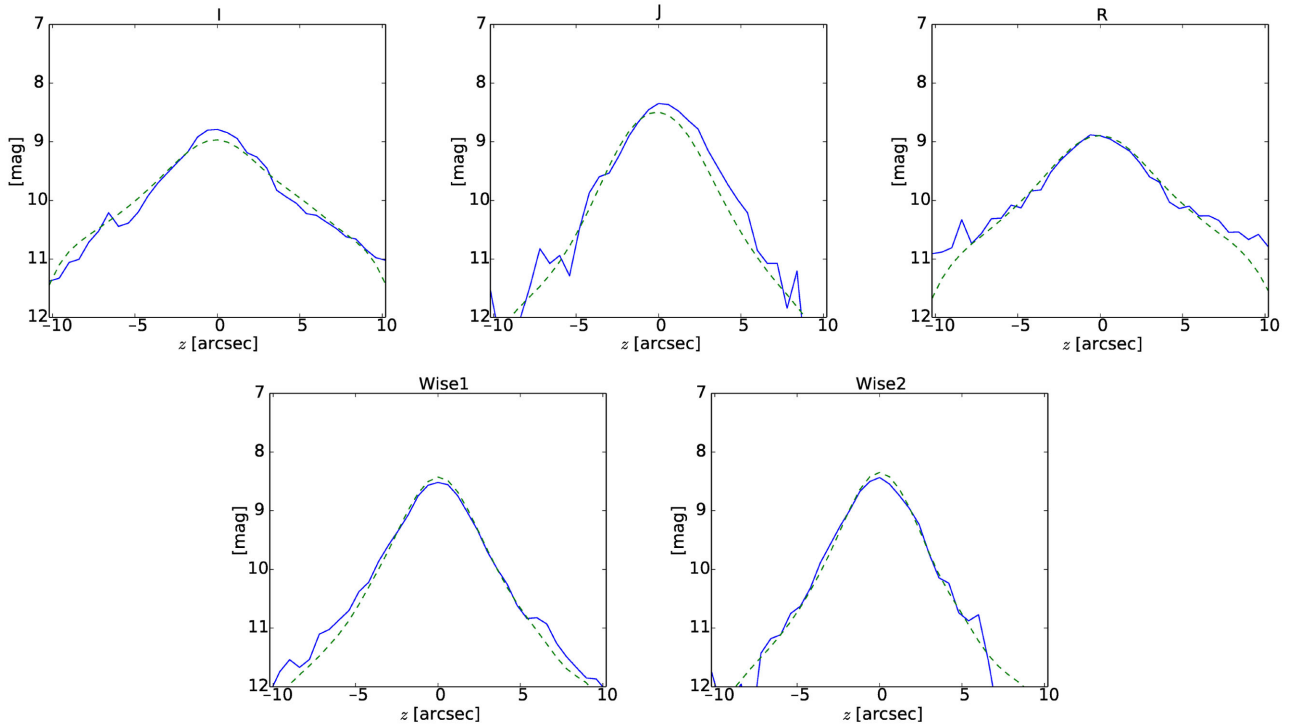

Figure 13. Profile of a vertical slice of UGC 7321. The profile was taken at a distance of 28.4 arcsec from the centre of the galaxy. Solid lines represent the observation and dashed lines the simulated galaxy. The zero-point is uncalibrated.

Astronomy Department, Krieger School of Arts and Sciences for this appointment.

PCK thanks the directors of these same institutions and his local hosts Ron Allen, Ken Freeman and Johan Knapen for hospitality and support during many work visits over the years, of which most were directly or indirectly related to the research presented in this series of articles.

Work visits by SPCP and PCK have been supported by an annual grant from the Faculty of Mathematics and Natural Sciences of the University of Groningen to PCK accompanying of his distinguished Jacobus C. Kapteyn professorhip and by the Leids Kerkhoven–Bosscha Fonds. PCK's work visits were also supported by an annual grant from the Area of Exact Sciences of the Netherlands Organization for Scientific Research (NWO) in compensation for his membership of its Board.

REFERENCES

Abe F. et al., 1999, AJ, 118, 261
Baes M., Dejonghe H., 2001a, MNRAS, 326, 722
Baes M., Dejonghe H., 2001b, MNRAS, 326, 733
Baes M. et al., 2003, MNRAS, 343, 1081
Baes M., Verstappen J., de Looze I., Fritz J., Saftly W., Vidal Pérez E., Stalevski M., Valcke S., 2011, ApJS, 196, 22
Bianchi S., 2007, A&A, 471, 765
Binney J., Tremaine S., 1987, Galactic Dynamics. Princeton Univ. Press, Princeton, NJ
Bland-Hawthorn J., Vlajić M., Freeman K. C., Draine B. T., 2005, ApJ, 629, 239
Byun Y.-I., 1992, PhD thesis, Austral. Nat. Univ., Canberra
Carignan C., 1983, PhD thesis, Austral. Nat. Univ., Canberra
Comerón S. et al., 2011, ApJ, 741, 28
Dalcanton J. J., Yoachim P., Bernstein R. A., 2004, ApJ, 608, 189
Dale D. A. et al., 2009, ApJ, 703, 517
de Geyter G., Baes M., Fritz J., Camps P., 2013, A&A, 550, A74
De Geyter G., Baes M., Camps P., Fritz J., de Looze I., Hughes T. M., Viaene S., Gentile G., 2014, MNRAS, 441, 869
de Grijs R., Peletier R. F., 1997, A&A, 320, L21
de Jong R. S., 1996, A&A, 313, 45
de Looze I. et al., 2012, MNRAS, 427, 2797
de Souza R. E., Dos Anjos S., 1987, A&AS, 70, 465
Engelbracht C. W., Rieke G. H., Gordon K. D., Smith J.-D. T., Werner M. W., Moustakas J., Willmer C. N. A., Vanzi L., 2008, ApJ, 678, 804
Erwin P., Pohlen M., Beckman J. E., 2008, AJ, 135, 20
Fathi K., Allen M., Boch T., Hatziminaoglou E., Peletier R. F., 2010, MNRAS, 406, 1595
Florido E., Battaner E., Guijarro A., Garzón F., Jiménez-Vicente J., 2001, A&A, 378, 82
Florido E., Battaner E., Guijarro A., Garzón F., Castillo-Morales A., 2006, A&A, 455, 467
Gadotti D. A., 2009, MNRAS, 393, 1531
Graham A. W., de Blok W. J. G., 2001, ApJ, 556, 177
Jarvis B. J., 1986, AJ, 91, 65
Kregel M., van der Kruit P. C., de Grijs R., 2002a, MNRAS, 334, 646
Kregel M., van der Kruit P. C., de Grijs R., 2002b, MNRAS, 334, 646
Lauberts A., 1982, ESO/Uppsala survey of the ESO(B) atlas. ESO, Garching
Lauberts A., Valentijn E. A., 1988, ESO Conf. Workshop Proc. Vol. 28, Astronomy from large databases: Scientific objectives and methodological approaches. European Southern Observatory, Garching, Germany, p. 37
MacLachlan J. M., Matthews L. D., Wood K., Gallagher J. S., 2011, ApJ, 741, 6
Matthews L. D., Gallagher J. S., III, van Driel W., 1999, AJ, 118, 2751
Morales-Luis A. B., Sánchez Almeida J., Aguerri J. A. L., Muñoz-Tuñón C., 2011, ApJ, 743, 77
Narayan C. A., Jog C. J., 2002, A&A, 390, L35

O'Brien J. C., Freeman K. C., van der Kruit P. C., 2010, A&A, 515, A63
Pohlen M., Zaroubi S., Peletier R. F., Dettmar R.-J., 2007, MNRAS, 378, 594
Radburn-Smith D. J. et al., 2011, ApJS, 195, 18
Roennback J., Bergvall N., 1995, A&A, 302, 353
Rossa J., Dettmar R.-J., 2003, A&A, 406, 505
Schlafly E. F., Finkbeiner D. P., 2011, ApJ, 737, 103
Schlegel D. J., Finkbeiner D. P., Davis M., 1998, ApJ, 500, 525
Sheth K. et al., 2010, PASP, 122, 1397
Sorce J. G., Tully R. B., Courtois H. M., 2012, ApJL, 758, L12
van der Kruit P. C., 1979, A&AS, 38, 15
van der Kruit P. C., 1988, A&A, 192, 117
van der Kruit P. C., 2007, A&A, 466, 883
van der Kruit P. C., Freeman K. C., 2011, ARA&A, 49, 301
van der Kruit P. C., Searle L., 1981, A&A, 95, 105
van der Kruit P. C., Jiménez-Vicente J., Kregel M., Freeman K. C., 2001, A&A, 379, 374
Wainscoat R. J., 1986, PhD thesis, Austr. Nat. Univ., Canberra
Wall M., 1996, Mech. Engin. Dept., MIT, 87, 54. Available at: lancet.mit.eda/ga/
Xilouris E. M., Byun Y. I., Kylafis N. D., Paleologou E. V., Papamastorakis J., 1999, A&A, 344, 868

SUPPORTING INFORMATION

Additional Supporting Information may be found in the online version of this article:

Appendix A. Tabular material.
(http://www.mnras.oxfordjournals.org/lookup/suppl/doi:10.1093/mnras/stw2100/-/DC1).

Please note: Oxford University Press is not responsible for the content or functionality of any supporting materials supplied by the authors. Any queries (other than missing material) should be directed to the corresponding author for the article.

This paper has been typeset from a TEX/LATEX file prepared by the author.